

Density determination of liquid iron-nickel-sulfur at high pressure

SAORI I. KAWAGUCHI^{1,2,*}†, GUILLAUME MORARD^{3,4}, YASUHIRO KUWAYAMA⁵, KEI HIROSE^{2,5},
NAOHISA HIRAO¹, AND YASUO OHISHI¹

¹Japan Synchrotron Radiation Research Institute, SPring-8, 1-1-1 Kouto, Sayo, Hyogo 679-5198, Japan

²Earth-Life Science Institute, Tokyo Institute of Technology, 2-12-1 Ookayama, Meguro-ku, Tokyo 152-8550, Japan

³Sorbonne Université, Institut de Minéralogie, de Physique des Matériaux et de Cosmochimie, IMPMC, Museum National d'Histoire Naturelle, UMR CNRS, 7590 Paris, France

⁴Université Grenoble Alpes, Université Savoie Mont Blanc, CNRS, IRD, IFSTTAR, ISTERre, 38000 Grenoble, France

⁵Department of Earth and Planetary Science, The University of Tokyo, 7-3-1 Hongo, Bunkyo-ku, Tokyo 113-0033, Japan

ABSTRACT

The density of liquid iron-nickel-sulfur ($\text{Fe}_{46.5}\text{Ni}_{28.5}\text{S}_{25}$) alloy was determined at pressures up to 74 GPa and an average temperature of 3400 K via pair distribution function (PDF) analysis of synchrotron X-ray diffraction (XRD) data obtained using laser-heated diamond-anvil cells. The determined density of liquid $\text{Fe}_{46.5}\text{Ni}_{28.5}\text{S}_{25}$ at 74 GPa and 3400 K is 8.03(35) g/cm³, 15% lower than that of pure liquid Fe. The obtained density data were fitted to a third-order Vinet equation of state (EoS), and the determined isothermal bulk modulus and its pressure derivative at 24.6 GPa are $K_{\text{TPF}} = 110.5(250)$ GPa and $K'_{\text{TPF}} = 7.2(25)$, respectively, with a fixed density of $r_{\text{Pr}} = 6.43$ g/cm³ at 24.6 GPa. The change in the atomic volume of $\text{Fe}_{46.5}\text{Ni}_{28.5}\text{S}_{25}$ upon melting was found to be ~10% at the melting temperature, a significantly larger value than that of pure Fe (~3%). Combined with the above EoS parameters and the thermal dependence reported in the literature, our data were extrapolated to the outer core conditions of the Earth. Assuming that S is the only light element and considering the range of suggested Ni content, we estimated a 5.3–6.6 wt% S content in the Earth's outer core.

Keywords: Liquid iron alloy, high pressure, Fe_3S , Earth's outer core; Physics and Chemistry of Earth's Deep Mantle and Core

INTRODUCTION

The liquid outer core of the Earth primarily comprises iron–nickel (Fe–Ni) alloyed with lighter elements. Recent measurements of the density contrast between the liquid outer core and pure liquid Fe were estimated to be 7.6%, assuming an adiabatic temperature profile with an inner core boundary temperature of 5400 K (Kuwayama et al. 2020). Both the nature and number of light elements in the core have remained to be the two biggest enigmas in Earth sciences for more than 60 years (Birch 1961). In this study, we focus on sulfur (S) as a potential light element in the Earth's core. S has a high solubility in liquid Fe at low pressures (Fei et al. 1997, 2000; Li et al. 2001; Stewart et al. 2007) and is missing in the mantle compared with other volatile elements (Murthy and Hall 1970). Owing to its high volatility, S was limited to ~1.7 wt% in core composition models (Dreibus and Palme 1996). However, recently, high-pressure partitioning experiments revised this value to >6wt% (Mahan et al. 2017). Therefore, from a geochemical perspective, S can be the primary light element in the Earth's core.

The density and sound velocity of the Earth's liquid outer core can be obtained from seismic observations such as the Preliminary Reference Earth Model (PREM, Dziewonski and Anderson 1981). Recently, we determined the sound velocity of liquid Fe–Ni–S alloys at pressures up to 52 GPa in diamond-anvil

cells (DACs) using high-resolution inelastic X-ray scattering (Kawaguchi et al. 2017a). Moreover, we discussed the S content in the Earth's outer core based on sound velocity data and demonstrated the compatibility of seismic data using 5.8–7.5 wt% S in the Earth's outer core, suggesting that S is the primary light element in the Earth's core. To complete this study, we performed density measurements of liquid Fe–S alloys at pressures corresponding to those in the Earth's core.

The density of liquid Fe alloys under extreme conditions was successfully determined using Paris-Edinburgh press and DAC via pair distribution function analysis of liquid diffuse signals in X-ray diffraction (XRD) patterns (Eggert et al. 2002; Morard et al. 2013, 2018; Kuwayama et al. 2020). Herein, we use this method to determine the density of liquid $\text{Fe}_{46.5}\text{Ni}_{28.5}\text{S}_{25}$ in DAC at pressures up to 70 GPa and an average temperature of 3400 K. Furthermore, we employ our findings to construct the isothermal equation of state (EoS).

METHODS

We determined the density of liquid $\text{Fe}_{46.5}\text{Ni}_{28.5}\text{S}_{25}$ via XRD measurements at the BL10XU beamline of SPring-8 (Hirao et al. 2020). $\text{Fe}_{46.5}\text{Ni}_{28.5}\text{S}_{25}$ synthesized in a multi-anvil apparatus was used as the samples in all runs. The sample composition was determined using field emission-electron probe microanalysis before loading. The sample pellets were cut into pieces 30–50 μm in diameter and 10 μm thick. Samples were loaded into a sample hole drilled in a rhenium gasket with a pressure medium [a dry potassium chloride (KCl) powder]. The samples were compressed to the pressures of interest using single-crystal diamond anvils with 300 μm culets. Then, they were heated using a double-sided laser-heating system to minimize the axial temperature gradient. The heating spot sizes on the samples were 25–40 μm.

* E-mail: saoi.kawaguchi@spring8.or.jp. Orcid 0000-0003-0970-7144

† Special collection papers can be found online at <http://www.minsocam.org/MSA/AmMin/special-collections.html>.

TABLE 1. *P-T* conditions, unit-cell volumes of KCl B2, and the obtained calculation properties of $\text{Fe}_{47}\text{Ni}_{28}\text{S}_{25}$

Run no.	<i>P</i> (GPa)	<i>T</i> (K)	KCl volume (\AA^3)	ρ (g/cm^3)	r_{min} (\AA)	ρ_0 (atoms/ \AA^3) $\times 10^{-2}$	BG factor	χ^2
X-ray energy: 30 keV								
1	33.8(12)	3200	35.79(4)	7.035	1.59	8.333	0.941	0.127
2	44.0(14)	3900	33.77(2)	7.342	1.54	8.697	0.954	0.176
3	55.9(12)	3200	30.95(5)	7.510	1.60	8.897	0.924	0.924
4	59.1(12)	3500	30.60(3)	7.639	1.52	9.048	0.905	0.103
5	69.5(12)	3200	29.00(1)	7.872	1.58	9.324	0.911	0.167
6	70.4(14)	3700	29.12(9)	7.771	1.62	9.230	0.902	0.344
7	74.2(14)	3700	28.67(12)	8.027	1.66	9.508	0.900	1.048
X-ray energy: 50 keV								
8	24.6(10)	2700	38.64(14)	6.434	1.66	7.621	0.926	0.358
9	37.0(13)	3500	35.24(13)	6.852	1.74	8.116	0.964	0.188

The temperature was measured using a spectroradiometric method, the variation of which was $\sim 10\%$. The X-ray was monochromatized to 30 and 50 keV using liquid nitrogen-cooled Si(111) and Si(220) double crystals. The X-ray compound refractive lenses achieved a focus of $\sim 8 \mu\text{m}$ (H) $\times 8 \mu\text{m}$ (V) at 30 keV and $10 \mu\text{m}$ (H) $\times 12 \mu\text{m}$ (V) at 50 keV (full-width at half maximum), which were sufficiently small compared with the laser beam size. Two-dimensional (2D) XRD images were captured on a charge-coupled device detector (SMART APEX, Bruker AX) and X-ray flat-panel detector (XRD0822, PerkinElmer, Inc.) with an exposure time of 1–10 s. We used IPAnalyzer and PDIndexer (Seto et al. 2010) for the X-ray energy and camera-length calibration and one-dimensional (1D) integration calculation of 2D XRD images. The pressure was determined using the KCl unit-cell volume with high-temperature thermal EoS reported by Tateno et al. (2019). Additionally, we collected powder XRD patterns of $\text{Fe}_{46.5}\text{Ni}_{28.5}\text{S}_{25}$ at 1 atm in a temperature range of 100–400 K at the BL02B2 beamline of SPring-8 (Kawaguchi et al. 2017b). The X-ray energy was 30 keV using water-cooled Si(111) double crystals; XRD data were collected using multiple 1D detectors (MYTHEN 1K, Dectris) in the temperature range of 100–400 K. Note that 24.8 keV X-ray was used for the XRD data collection for structural refinement. We performed structural refinements by the Rietveld method using JANA2006 (Petříček et al. 2006). See the CIF (via Online Materials¹) for more information.

RESULTS

We conducted nine separate experiments to collect XRD data of $\text{Fe}_{46.5}\text{Ni}_{28.5}\text{S}_{25}$ at pressures up to 70 GPa. Table 1 lists the density, pressure, temperature, KCl unit-cell volume, and

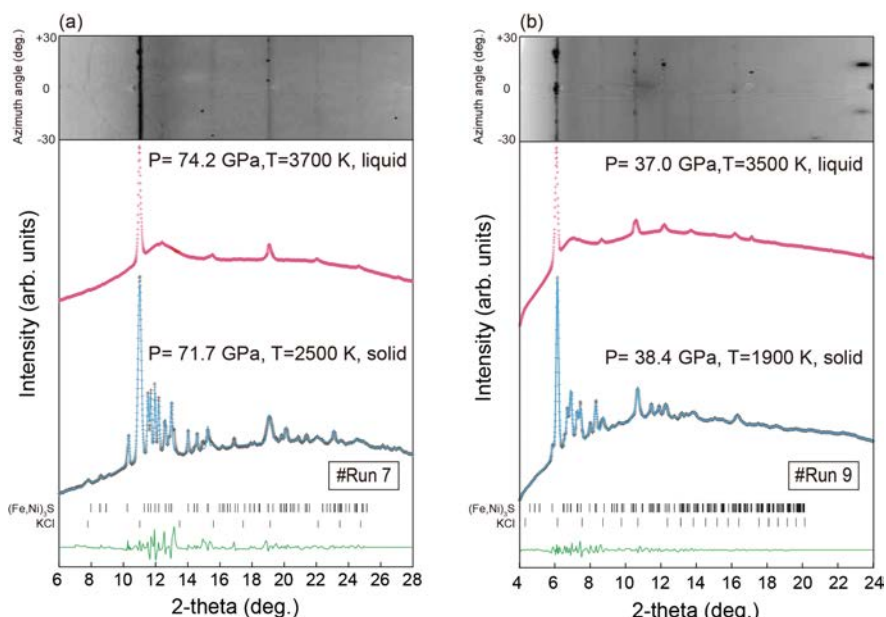
calculated properties. We obtained XRD data in the temperature range of 2700–3900 K, and the temperature effect was included in the analytical pressure error. We set an average temperature of 3400 K as the temperature condition in this study. All experiments were performed at temperatures higher than the predicted melting point of Fe_3S (Fei et al. 1997, 2000; Morard et al. 2008; Mori et al. 2017). We excluded liquid X-ray data containing major XRD peaks from solid Fe and other compounds.

The density of liquid $\text{Fe}_{46.5}\text{Ni}_{28.5}\text{S}_{25}$ was determined by pair distribution analysis. More information pertaining to this method is available in the literature (Morard et al. 2013). Figure 1 shows typical 1D and 2D XRD patterns of solid and liquid $\text{Fe}_{46.5}\text{Ni}_{28.5}\text{S}_{25}$ at 70 GPa (the highest pressure tested in this study) and 30 GPa using 30 keV X-rays. In the analysis, Bragg spots from the diamond anvils were masked. Figure 1 also shows the results of whole XRD pattern profile fitting using the Le Bail method of $(\text{Fe,Ni})_3\text{S}$ (space group: $\bar{I}4$) and KCl B2 (space group: $Pm\bar{3}m$). In the XRD patterns, the liquid sample exhibits broad halos. Both before and after melting, the signals were fitted using spline curves. The only halo peak intensity of the liquid sample, which is expressed as a function of the scattering angle $I_{\text{sample}}(\theta)$, was extracted from the measured XRD signal function after melting $I_{\text{mes}}(\theta)$ via the subtraction of the background signal function $I_{\text{bg}}(\theta)$. Herein, $I_{\text{bg}}(\theta)$ was obtained from the solid XRD signal before melting. The scattering angle 2θ can be transformed into scattering momentum (Q) with wavelength (λ) via $Q = 4\pi\sin\theta/\lambda$. Then, $I_{\text{sample}}(Q)$ can be written as:

$$I_{\text{sample}}(Q) = I_{\text{mes}}(Q) - bI_{\text{bg}}(Q) \quad (1)$$

where b is a background factor. In this study, we used Krogh-Moe–Norman normalization (Krogh-Moe 1956; Norman 1957; Morard et al. 2013) for processing $I_{\text{sample}}(Q)$ to structure factor $S(Q)$. Reduced pair distribution function $G(r)$ and pair distribution function $g(r)$ were calculated from $S(Q)$ using Fourier transform:

FIGURE 1. 1D XRD patterns of solid (gray symbols) and liquid (pink symbols) $\text{Fe}_{47}\text{Ni}_{28}\text{S}_{25}$ and 2D XRD patterns of liquid $\text{Fe}_{47}\text{Ni}_{28}\text{S}_{25}$ obtained at (a) ~ 74 GPa using 30 keV X-rays and (b) ~ 37 GPa using 50 keV X-rays. Blue and green lines indicate the whole pattern profile fitting results of $(\text{Fe,Ni})_3\text{S}$ (space group: $\bar{I}4$) and KCl B2 (space group: $Pm\bar{3}m$) using the Le Bail method and the differences between the observed and calculated profiles, respectively. (Color online.)



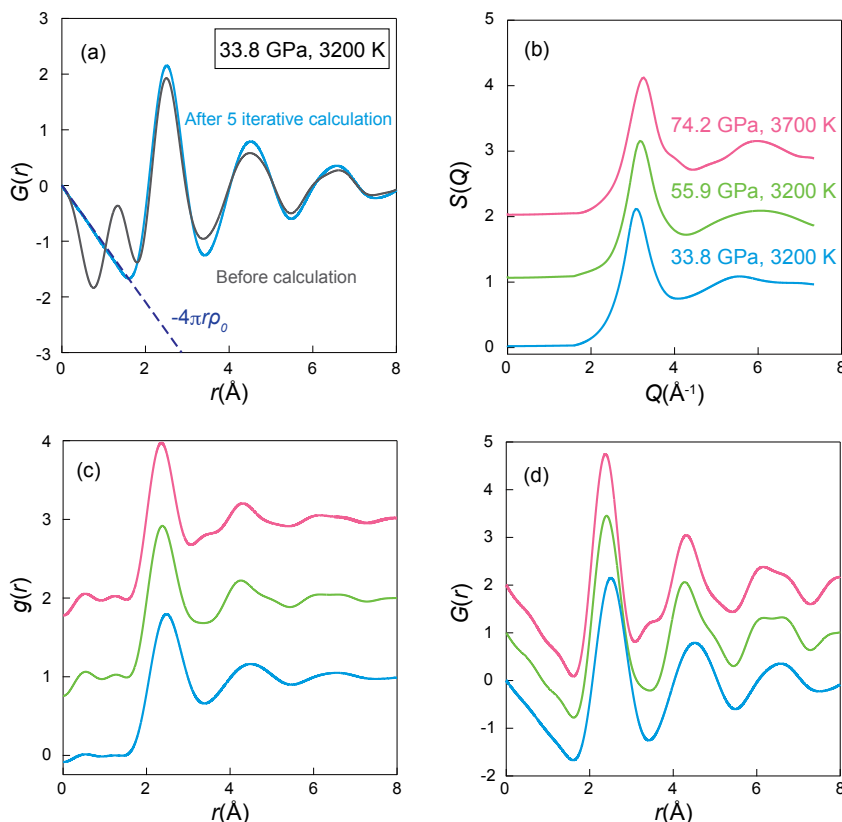


FIGURE 2. Typical Faber-Ziman structure factor $S(Q)$, reduced pair distribution function $G(r)$, and pair distribution function $g(r)$. (a) Comparison of $G(r)$ functions before and after five iterative optimization calculations; (b–d) typical $S(Q)$, $g(r)$, and $G(r)$ functions after optimization at 34, 56, and 74 GPa (light blue, light green, and pink lines, respectively). (Color online.)

$$G(r) = 4\pi r [\rho(r) - \rho_0] = \frac{2}{\pi} \int_0^{Q_{\max}} Q \{S(Q) - 1\} \sin(Qr) dQ \quad (2)$$

$$g(r) = G(r)/4\pi r \rho_0 + 1 \quad (3)$$

where r , $\rho(r)$, ρ_0 , and Q_{\max} are the radial distance from the atom, atomic density, average atomic density, and maximum scattering momentum in each data point, respectively. Figure 2 shows the typical $S(Q)$, $G(r)$, and $g(r)$ functions after completing the analytical calculations. Owing to the repulsive force of an atom from a reference point ($r = 0$), no atom should be closer than the first coordination shell r_{\min} . Therefore, in the range $0 < r < r_{\min}$, $G(r)$ can be represented as a linear function:

$$G(r) = -4\pi r \rho_0. \quad (4)$$

Using the above principle, it is necessary to integrate Equation 2 from $Q = 0$ to ∞ , which is not possible using experimental data. Additionally, $Q = 6\text{--}7 \text{\AA}^{-1}$ is the upper limit when using 30-keV X-rays because of the aperture angle of the DAC. Such a limited Q range produces ripples (Fig. 2a) in the distribution functions. To minimize these ripples in $G(r)$, which are attributed to the Q truncation effect, the difference between ideal $G(r) = -4\pi r \rho_0$ and $G(r) = G_0(r)$ directly obtained from the raw data (without iteration) was calculated in the range $0 < r < r_{\min}$:

$$\Delta G(r) = -4\pi r \rho_0 - G(r). \quad (5)$$

Then, the function was integrated from 0 to r_{\min} as the sum of the squares of the differences:

$$\chi^2(\rho_0, b) = \int_0^{r_{\min}} \Delta G_i(r)^2 dr. \quad (6)$$

To minimize χ^2 , background factors b and ρ_0 were determined.

The density of the liquid sample can then be expressed as:

$$\rho = \rho_0 \times M \quad (7)$$

where M is the average atomic weight. We determined the uncertainty of the calculated ρ_0 to be $\pm 3 \times 10^{-3} \text{ atoms/\AA}^3$ by considering the Q truncation effects. Herein, the bulk of runs for the XRD measurements were operated using 30 keV X-rays. Thus, the Q range was limited to $< 6\text{--}7 \text{\AA}^{-1}$, implying that only two oscillations could be observed for liquid Fe alloys. In run #9, using higher-energy X-rays at 50 keV, we successfully obtained data for a higher Q range of up to 10.5\AA^{-1} (Fig. 1). Furthermore, we examined the uncertainty in the ρ_0 determination using two oscillations compared with the data after the third oscillation, which we calculated to be $\pm 2.9 \times 10^{-3} \text{ atoms/\AA}^3$. This estimated uncertainty was consistent with that reported by Morard et al. (2013) and was confirmed via a similar examination using higher

Q range data at lower pressures with Paris–Edinburgh press. Similar to the method used by Morard et al. (2013), calculations were performed by shifting r_{\min} in steps of 0.1 Å. The ρ_0 fluctuation in $r = \pm 0.1$ Å was approximately $\pm 1 \times 10^{-3}$ atoms/Å³. We estimated the uncertainty of density in the present study to be 3.9×10^{-3} atoms/Å³, i.e., 0.349 g/cm³, for Fe_{46.5}Ni_{28.5}S₂₅.

The obtained density values were fitted using the third-order Vinet EoS.

$$(P - Pr) = K_{TPr} x^{2/3} (1 - x^{-1/3}) \times \exp \left[\frac{3}{2} (K'_{TPr} - 1) (1 - x^{-1/3}) \right] \quad (8)$$

where Pr , K_{TPr} , K'_{TPr} , and x are the reference pressure, isothermal bulk modulus, its first pressure derivative at reference pressure and 3400 K, and $x = \rho/\rho_{Pr,3400\text{ K}}$, respectively. A structural transition at ~20 GPa has been suggested for liquid Fe_{46.5}Ni_{28.5}S₂₅ from sound velocity determination (Kawaguchi et al. 2017a). Considering the structural transition below 20 GPa, we performed the fitting based on measured density data at the lowest pressure point. We derived the pressure dependence of the density of liquid Fe_{46.5}Ni_{28.5}S₂₅. The best fit for the compression curve of the density data yielded $K_{TPr} = 110.5(250)$ GPa and $K'_{TPr} = 7.2(25)$ with a fixed $\rho_{Pr,3400\text{ K}} = 6.434$ g/cm³ (Table 2). Figure 3 shows the confidence ellipsoid of the determined K_{TPr} and K'_{TPr} . As reported in Angel (2000), the confidence ellipsoid is expressed as:

$$\Delta = (K_{TPr}, K'_{TPr}) \begin{pmatrix} \sigma_{K_{TPr}, K_{TPr}} & \sigma_{K_{TPr}, K'_{TPr}} \\ \sigma_{K'_{TPr}, K_{TPr}} & \sigma_{K'_{TPr}, K'_{TPr}} \end{pmatrix}^{-1} \begin{pmatrix} K_{TPr} \\ K'_{TPr} \end{pmatrix} \quad (9)$$

with the covariance of K_{TPr} and K'_{TPr} , where Δ is the χ^2 distribution (here, $\Delta = 2.3$ for 1 σ level confidence with two degrees of freedom).

To characterize thermal expansion of Fe_{46.5}Ni_{28.5}S₂₅, we performed powder XRD measurements at 1 atm from 90 to 400 K. Figures 4a and 4b show temperature dependence of XRD pattern and structural refinement results via Rietveld analysis with high reliability ($R_{wp} = 2.79\%$, $R_l = 3.84\%$) at room temperature. These data indicate that the sample had no impurities. Tetragonal (Fe,Ni)₃S (space group: $I4$) was stable throughout the temperature range measured.

DISCUSSION

All density data and fitting results are summarized as a function of pressure in Figure 5. In Figure 5, we show the isothermal density profiles at 2700 and 3900 K, which are the minimum and maximum temperatures, respectively. Although the temperature conditions in the present study were slightly different in each run, the agreement of the fitting results and the present density data were within the estimated pressure and density errors. The present data show that the density of liquid Fe_{46.5}Ni_{28.5}S₂₅ increased from 6.434(349) g/cm³ at 24.6 GPa and 2700 K to 8.027(349) g/cm³ at 74.2 GPa and 3700 K. Figure 5 also shows the density profile of pure liquid Fe at 3400 K calculated from the EoS reported by Kuwayama et al. (2020). The difference between the densities of liquid Fe and liquid

TABLE 2. Fitting results using the Vinet equation of state

T_0 (K)	K_{TPr} (GPa)	K'_{TPr}	ρ_{Pr} (g/cm ³)	P_r (GPa)
3400	110.5(250)	7.2(25)	6.434	24.6

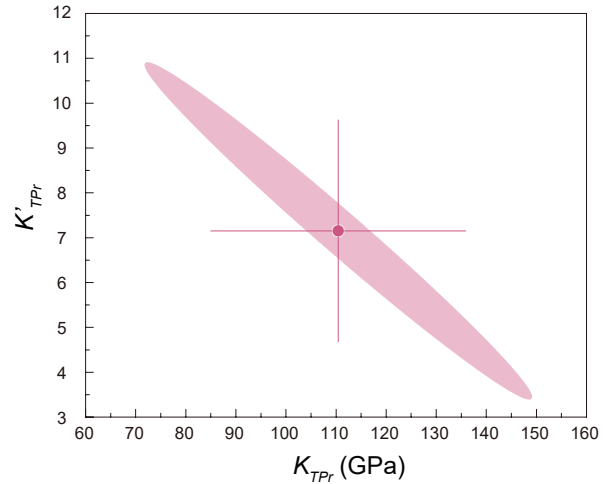


FIGURE 3. Confidence ellipsoid in K_{TPr} and K'_{TPr} for fitting using the third-order Vinet EoS with a 68.3% confidence level and $\Delta = 2.3$. The fitting result is shown as a circular symbol with errors of $K_{TPr} = 110.5(250)$ GPa and $K'_{TPr} = 7.2(25)$. (Color online.)

Fe_{46.5}Ni_{28.5}S₂₅ is 16% in the pressure range of 20–70 GPa.

Morard et al. (2013, 2018) and Terasaki et al. (2019) reported density measurement results for liquid Fe-(Ni)-S systems. Morard et al. (2013) performed Fe₇₆Ni₄S₂₀ measurements using laser-heated DACs, as done in this study; the average atomic mass in our study differed from theirs by only 4%. The results reported by Morard et al. (2013) and the present data are consistent within the margin of error.

However, although their temperatures were lower by >1300 K, Morard et al. (2018) and Terasaki et al. (2019) reported high compressibility at lower pressures (<20 GPa) than that obtained in the present study. This observation indicates the existence of a semimetallic to compact metallic structural transition, as discussed in Kawaguchi et al. (2017a) and other studies on treated Fe-S alloys (Nishida et al. 2011; Morard et al. 2007). Morard et al. (2008) suggested that covalent Fe-S bonds in liquid Fe-S transform to an interstitial metallic-like configuration, similar to Fe-Si at high pressures.

Figure 5 compares our results with the density profile at 3400 K and densities at 30 and 100 GPa near the melting temperatures of solid Fe₃S calculated using the EoS of Thompson et al. (2020). This comparison indicates that melting reduces the density of (Fe,Ni)₃S by ~9.3% at 30 GPa and 2000 K and 11.5% at 100 GPa at 2500 K, thereby indicating a 12–15% increase in the atomic volume. Although our sample included 28at% Ni, it produced only a 3% density difference. When melting pure Fe, Anderson and Isaak (2002) found that the atomic volume change was 1.2–1.3% at 330 GPa, a pressure condition corresponding to the inner core boundary. From recent compression experiments on pure solid hcp Fe (Dewaele et al. 2006) and pure liquid Fe (Kuwayama et al. 2020), the atomic volume changes were estimated to be 3% at 100 GPa and near the melting temperature, $T = 3000$ K. The results indicate that S increases the volume change when Fe alloys are melted. Figure 6 shows the crystal structure of Fe_{46.5}Ni_{28.5}S₂₅ at 1 atm

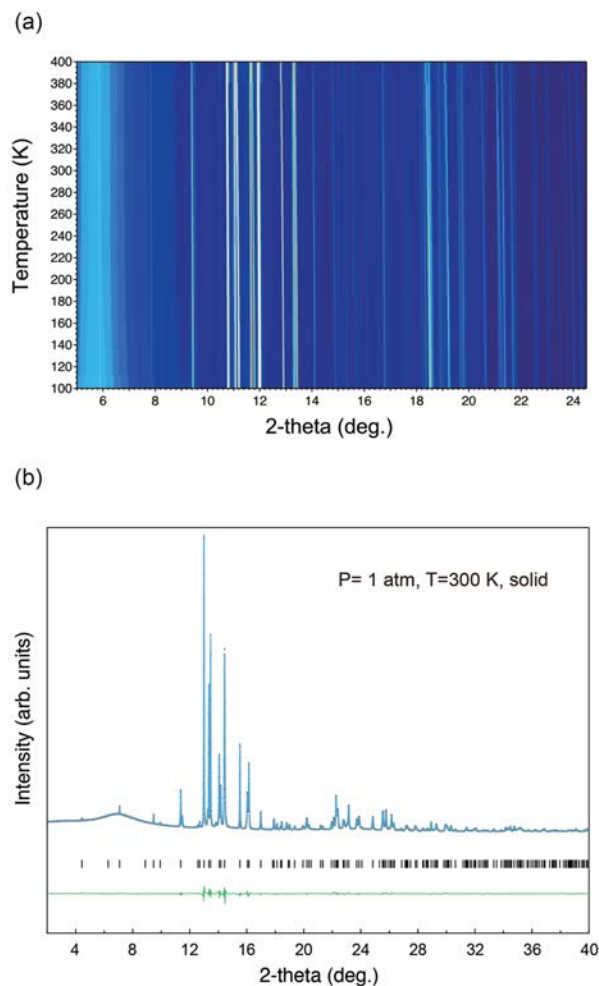


FIGURE 4. (a) Temperature dependence of powder XRD pattern of $\text{Fe}_{46.5}\text{Ni}_{28.5}\text{S}_{25}$ in the temperature range 100–400 K at 1 atm using 30 keV X-rays; (b) XRD pattern of $\text{Fe}_{46.5}\text{Ni}_{28.5}\text{S}_{25}$ at room temperature using 24.8 keV X-rays and its Rietveld analysis. (Color online.)

and 300 K with anisotropic displacement ellipsoids at the 80% probability level drawn using the VESTA (Momma and Izumi 2011). Figure 7 plots variations of unit-cell parameters a and c and unit-cell volume V as a function of temperature. Cell parameters increase almost linearly with increasing temperature; however, the c axis exhibits a higher expansion rate than the a axis. Sun et al. (2004) attributed the anisotropy of melting to that of the crystal structure based on molecular dynamics (MD) simulation results. They revealed that bcc Fe has higher mobility and lower free energy of the solid-liquid interface than those of fcc Fe. In addition, mobility along the (100) orientation of bcc Fe is larger than those along its (111) and (110) orientations. Hence, the large atomic volume change related to melting of $\text{Fe}_{46.5}\text{Ni}_{28.5}\text{S}_{25}$ was possibly a result of the large anisotropy in thermal vibration of the bcc Fe_3S structure (space group $I\bar{4}$) compared with face-centered cubic and hexagonal close-packed Fe. Structural refinement and MD simulation of the solid materials immediately before their melting and precise

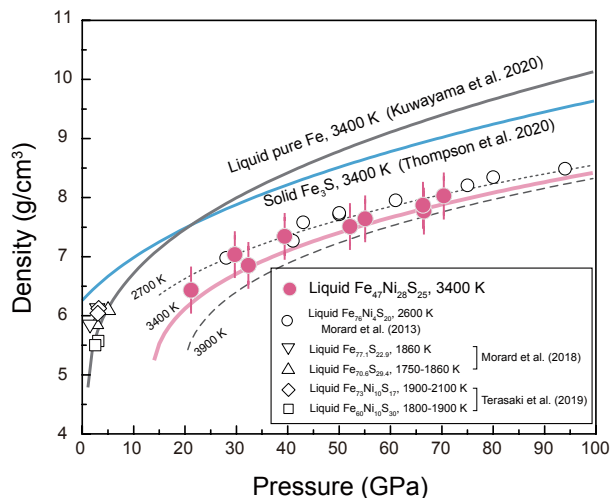


FIGURE 5. Densities of liquid and solid Fe-Ni-S and Fe-S alloys and Fe. The data of $\text{Fe}_{46.5}\text{Ni}_{28.5}\text{S}_{25}$ obtained in this study are represented by solid pink circles. The pink line indicates the fitting result using Vinet EoS. Previous measurements using a similar XRD method for liquid $\text{Fe}_{76}\text{Ni}_{4}\text{S}_{20}$ (Morard et al. 2013), XRD method in Paris-Edinburgh press for liquid $\text{Fe}_{77.1}\text{S}_{22.9}$ and $\text{Fe}_{70.6}\text{S}_{29.4}$ (Morard et al. 2018), and X-ray absorption method in multi-anvil press (Terasaki et al. 2019) for liquid $\text{Fe}_{73}\text{Ni}_{10}\text{S}_{17}$ and $\text{Fe}_{60}\text{Ni}_{10}\text{S}_{30}$ are represented by the open diamonds and squares, respectively. The gray and light blue lines indicate the calculated densities of liquid Fe using the EoS in Kuwayama et al. (2020) and solid Fe_3S using the EoS in Thompson et al. (2020), respectively, at 3400 K. Dotted and broken lines indicate the calculated isothermal density profiles of liquid $\text{Fe}_{46.5}\text{Ni}_{28.5}\text{S}_{25}$ at 2700 and 3900 K. (Color online.)

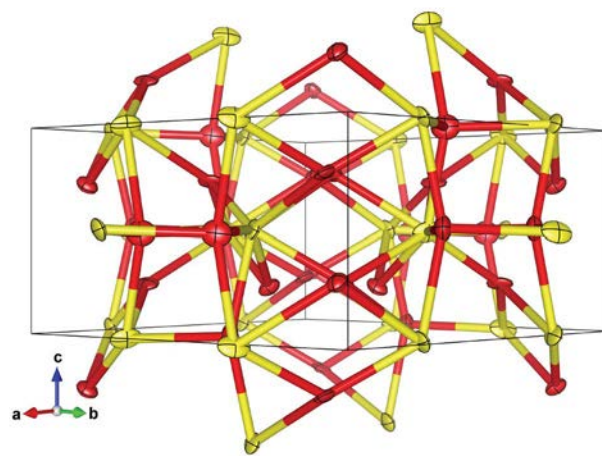


FIGURE 6. Crystal structure of $\text{Fe}_{46.5}\text{Ni}_{28.5}\text{S}_{25}$ at 300 K with anisotropic displacement ellipsoids at 80% probability level. Red and yellow symbols indicate the thermal vibrations of Fe/Ni and S, respectively. (Color online.)

structural characterization of the liquid and amorphous materials via pair distribution analyses using higher-energy X-rays should be attempted in future work.

IMPLICATIONS

The density deficit in the outer core in terms of pure liquid Fe was estimated to be 7.5–7.6% (Kuwayama et al. 2020). To

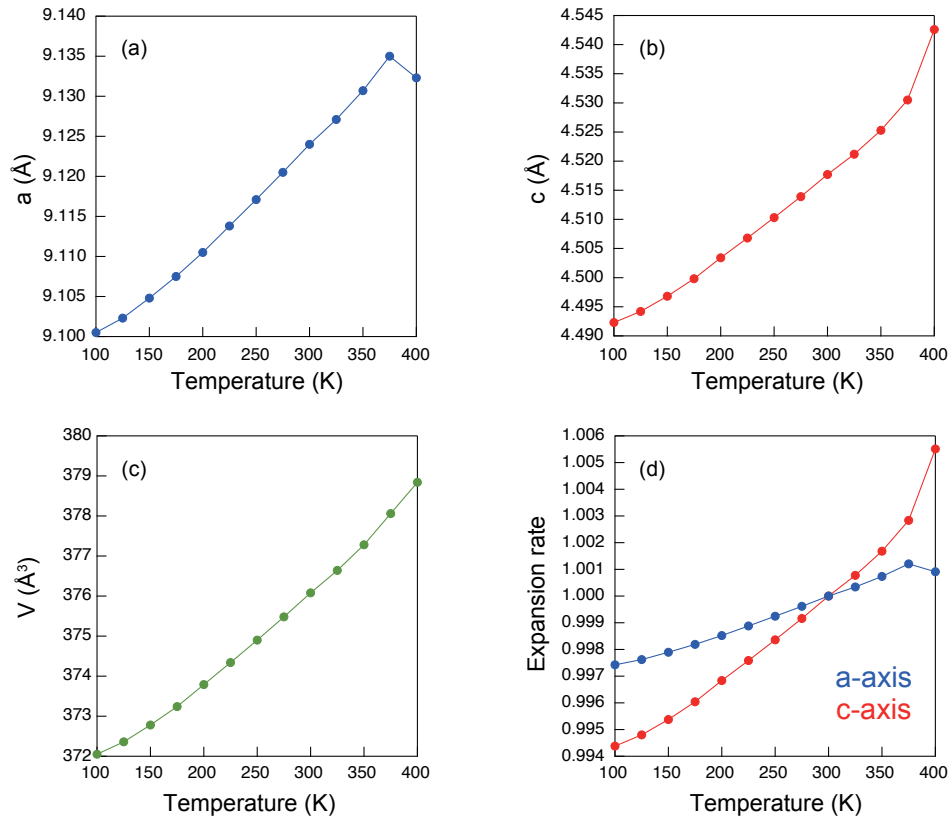


FIGURE 7. Temperature dependencies of unit-cell parameters (a) a (blue), (b) c (red), and (c) unit-cell volume V (green); (d) a comparison of the expansion rates of the a and c axes based on the values at 300 K. (Color online.)

discuss the density of the Earth's outer core, we used a constant αK_T relationship:

$$P(\rho, T) = P(\rho, T_0) + \Delta P_{\text{th}} \quad (10)$$

$$\Delta P_{\text{th}} = \alpha K_T (T - T_0) \quad (11)$$

where α , K_T , and T_0 are the thermal expansion coefficient, isothermal bulk modulus, and reference temperature (3400 K), respectively. Additionally, $\alpha \times K_T$ can be considered as constant from reference pressure and temperature to the pressure-temperature (P - T) condition of interest ($\alpha \times K_T = \alpha_{\text{pr}} \times K_{\text{TPr}}$). Assuming that the temperature effect on the sound velocities can be negligible, we refitted the sound velocity data of Kawaguchi et al. (2017a) using $\rho_{\text{Pr}, 3400 \text{ K}}$ determined herein, yielding an adiabatic bulk modulus $K_{\text{SPr}} = 186.8 \text{ GPa}$ at 24.6 GPa and 3400 K. The relation between K_{SPr} and K_{TPr} can be expressed as $K_{\text{SPr}}/K_{\text{TPr}} = (1 + \alpha_{\text{pr}} \times \gamma_{\text{pr}} \times T_{\text{pr}})$, where γ_{pr} of pure Fe is from Kuwayama et al. (2020). Combination of K_{SPr} , K_{TPr} , and γ_{pr} yielded $\alpha_{\text{pr}} \times K_{\text{TPr}} = 1.18 \times 10^{-2} \text{ GPa/K}$.

We calculated the adiabatic temperature as follows:

$$T = T_{\text{ref}} \exp \left[\gamma_{\text{ref}} \left(1 - \frac{\rho_{\text{ref}}}{\rho} \right) \right] \quad (12)$$

where T_{ref} is the reference temperature, and γ_{ref} is the Grüneisen parameter at 24.6 GPa and T_{ref} . We calculated γ_{ref} for pure Fe based on the data of Kuwayama et al. (2020). In Figure 8, the densities of liquid Fe-Ni-S alloys and Fe are plotted

along the adiabatic temperature profiles corresponding to the temperatures at the core-mantle boundary (CMB), i.e., $T_{\text{CMB}} = 3600$ and 4300 K ($T_{\text{ref}} = 2459$ and 2812 K , respectively). The obtained density profiles appear to differ from previous shock experimental results (Huang et al. 2013). Conversely, our results are consistent with the density calculated from the sound velocity data reported by Kawaguchi et al. (2017a), which was recalculated using thermoelastic parameters of pure Fe (Kuwayama et al. 2020). We also calculated the density of liquid Fe_3S , assuming that Ni has little effect on the thermal elastic parameters (e.g., Kawaguchi et al. 2017a). Finally, assuming ideal mixing with pure Fe and S as the only light element in the Earth's core, the density profile of the outer core is best explained using 5.7–6.6 wt% S with Ni and 5.3–6.2 wt% S without Ni. This estimation is compatible with our sound velocity measurements, which suggest a volume of 5.8–7.5 wt% S in the Earth's outer core.

S is considered a dominant candidate for lighter components in the martian core. The S content of Mars is approximately 10.6–16.2 wt%, estimated from martian-origin shergottite, nakhlite, and chassignite meteorites (e.g., Dreibus and Wanke 1985). A (partially) molten martian core has been reported using observed large Love number k_2 (e.g., Yoder et al. 2003). In Figure 9, we show the isothermal density profiles of $\text{Fe}_{46.5}\text{Ni}_{128.5}\text{S}_{25}$ (16 wt% S) and pure Fe (0 wt% S) at 1500, 1900, and 2300 K in the pressure range corresponding to that of the martian core

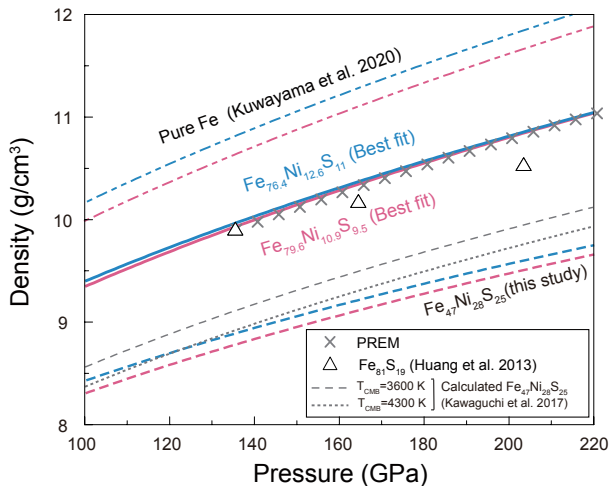


FIGURE 8. Densities of liquid Fe-Ni-S alloys and Fe along adiabats with $T_{\text{CMB}} = 3600$ and 4300 K (blue and pink curves, respectively). Density profiles of $\text{Fe}_{46.5}\text{Ni}_{28.5}\text{S}_{25}$ calculated from the present results and pure Fe (Kuwayama et al. 2020) are shown with broken and dashed lines, respectively. Solid blue and red curves indicate the best fits to PREM (crosses) with liquid $\text{Fe}_{76.4}\text{Ni}_{12.6}\text{S}_{11}$ ($T_{\text{CMB}} = 3600$ K) and $\text{Fe}_{79.6}\text{Ni}_{10.9}\text{S}_{9.5}$ ($T_{\text{CMB}} = 4300$ K), respectively. The calculated density profiles of $\text{Fe}_{46.5}\text{Ni}_{28.5}\text{S}_{25}$ from the sound velocity data of Kawaguchi et al. (2017a) are shown by gray dashed ($T_{\text{CMB}} = 3600$ K) and dotted ($T_{\text{CMB}} = 4300$ K) lines. (Color online.)

(Tsuji et al. 2013). Mars exploration lander, InSight, landed on Mars in 2018. Additionally, ExoMars 2022 will be launched in the denoted year. InSight's rotation and interior structure experiment (Folkner et al. 2018), seismometer data (Giardini et al. 2020), and ExoMars' lander radio-science experiment (Péters et al. 2020) will provide additional information about the interior structure of Mars and its core. Our density and sound velocity data may help better understand the martian core and its thermal evolution.

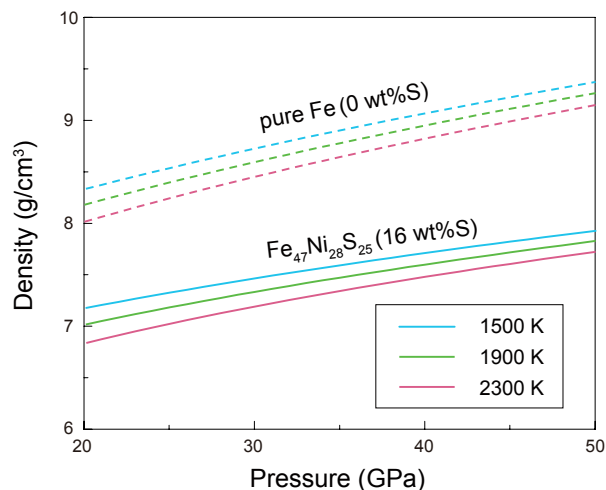


FIGURE 9. Isothermal density profiles of liquid $\text{Fe}_{46.5}\text{Ni}_{28.5}\text{S}_{25}$ (16 wt% S) and pure Fe (0 wt% S) in the pressure range corresponding to the martian core at 1500 (blue), 1900 (green), and 2300 K (pink). (Color online.)

ACKNOWLEDGMENTS AND FUNDING

We thank Y. Nakajima for sample preparation and Y. Higo, Y. Tange, and S. Kawaguchi for their fruitful discussion and help in analysis. R. Sinmyo, H. Xu, S. Kamada, and an anonymous referee were helpful to improve the manuscript. XRD measurements using DAC and at ambient pressures were performed at the BL10XU (proposals no. 2014A0080, 2014A1127, 2016A1846, 2016B1954, 2016B1955, 2017B1977, 2018A2062, 2018B2109, 2019A1381, 2019B2094) and BL02B2 beamlines (proposals no. 2019B2086) of Spring-8.

REFERENCES CITED

- Anderson, O.L., and Isaak, D.G. (2002) Another look at the core density deficit of Earth's outer core. *Physics of the Earth and Planetary Interiors*, 131, 19–27.
- Angel, R.J. (2000) Equations of state. *Reviews in Mineralogy and Geochemistry*, 41, 35–59.
- Birch, F. (1961) The velocity of compressional waves in rocks to 10 kilobars: 2. *Journal of Geophysical Research*, 66, 2199–2224.
- Dewaele, A., Loubeyre, P., Ocellli, F., Mezouar, M., Dorogokupets, P., and Torrent, M. (2006) Quasihydrostatic equation of state of iron above 2 Mbar. *Physical Review Letters*, 97, 215504.
- Dreibus, G., and Palme, H. (1996) Cosmochemical constraints on the sulfur content in the Earth's core. *Geochimica et Cosmochimica Acta*, 60, 1125–1130.
- Dreibus, G., and Wanke, H. (1985) Mars, a volatile-rich planet. *Meteoritics*, 20, 367–381.
- Dziewonski, A.M., and Anderson, D.L. (1981) Preliminary reference Earth model. *Physics of the Earth and Planetary Interiors*, 25, 297–356.
- Eggert, J.H., Weck, G., Loubeyre, P., and Mezouar, M. (2002) Quantitative structure factor and density measurements of high-pressure fluids in diamond anvil cells by X-ray diffraction: Argon and water. *Physical Review B*, 65, 174105.
- Fei, Y., Bertka, C.M., and Finger, L.W. (1997) High-pressure iron-sulfur compound, Fe_3S_2 , and melting relations in the Fe–FeS system. *Science*, 275, 1621–1623.
- Fei, Y., Li, J., Bertka, C.M., and Prewitt, C.T. (2000) Structure type and bulk modulus of Fe_3S , a new iron-sulfur compound. *American Mineralogist*, 85, 1830–1833.
- Folkner, W.M., Dehant, V., Le Maistre, S., Yseboodt, M., Rivoldini, A., Van Hoolst, T., Asmar, S.W., and Golombek, M.P. (2018) The rotation and interior structure experiment on the InSight mission to Mars. *Space Science Reviews*, 214, 100.
- Giardini, D., Lognonné, P., Banerdt, W.B., Pike, W.T., Christensen, U., Ceylan, S., Clinton, J.F., van Driel, M., Stähler, S.C., Böse, M., and others (2020) The seismicity of Mars. *Nature Geoscience*, 13, 205–212.
- Hirao, N., Kawaguchi, S.I., Hirose, K., Shimizu, K., Ohtani, E., and Ohishi, Y. (2020) New developments in high-pressure X-ray diffraction beamline for diamond anvil cell at SPring-8. *Matter and Radiation at Extremes*, 5, 018403.
- Huang, H., Wu, S., Hu, X., Wang, Q., Wang, X., and Fei, Y. (2013) Shock compression of Fe-FeS mixture up to 204 GPa. *Geophysical Research Letters*, 40, 687–691.
- Kawaguchi, S.I., Nakajima, Y., Hirose, K., Komabayashi, T., Ozawa, H., Tateno, S., Kuwayama, Y., Tsutsui, S., and Baron, A.Q. (2017a) Sound velocity of liquid Fe-Ni-S at high pressure. *Journal of Geophysical Research: Solid Earth*, 122, 3624–3634.
- Kawaguchi, S., Takemoto, M., Osaka, K., Nishibori, E., Moriyoshi, C., Kubota, Y., Kuroiwa, Y., and Sugimoto, K. (2017b) High-throughput powder diffraction measurement system consisting of multiple MYTHEN detectors at beamline BL02B2 of SPring-8. *The Review of Scientific Instruments*, 88, 085111.
- Krogh-Moe, J. (1956) A method for converting experimental X-ray intensities to an absolute scale. *Acta Crystallographica*, 9, 951–953.
- Kuwayama, Y., Morard, G., Nakajima, Y., Hirose, K., Baron, A.Q.R., Kawaguchi, S.I., Tsuchiya, T., Ishikawa, D., Hirao, N., and Ohishi, Y. (2020) Equation of state of liquid iron under extreme conditions. *Physical Review Letters*, 124, 165701.
- Li, J., Fei, Y., Mao, H.K., Hirose, K., and Shieh, S.R. (2001) Sulfur in the Earth's inner core. *Earth and Planetary Science Letters*, 193.
- Mahan, B., Siebert, J., Pringle, E.A., and Moynier, F. (2017) Elemental partitioning and isotopic fractionation of Zn between metal and silicate and geochemical estimation of the S content of the Earth's core. *Geochimica et Cosmochimica Acta*, 196, 252–270.
- Momma, K., and Izumi, F. (2011) VESTA 3 for three-dimensional visualization of crystal, volumetric and morphology data. *Journal of Applied Crystallography*, 44, 1272–1276.
- Morard, G., Sanloup, C., Fiquet, G., Mezouar, M., Rey, N., Poloni, R., and Beck, P. (2007) Structure of eutectic Fe–FeS melts to pressures up to 17 GPa: Implications for planetary cores. *Earth and Planetary Science Letters*, 263, 128–139.
- Morard, G., Andrault, D., Guignot, N., Sanloup, C., Mezouar, M., Petitgirard, S., and Fiquet, G. (2008) In situ determination of Fe–Fe₃S phase diagram and liquid structural properties up to 65 GPa. *Earth and Planetary Science Letters*, 272, 620–626.
- Morard, G., Siebert, J., Andrault, D., Guignot, N., Garbarino, G., Guyot, F., and Antonangeli, D. (2013) The Earth's core composition from high pressure density measurements of liquid iron alloys. *Earth and Planetary Science*

- Letters, 373, 169–178.
- Morard, G., Bouchet, J., Rivoldini, A., Antonangeli, D., Roberge, M., Boulard, E., Denoed, A., and Mezouar, M. (2018) Liquid properties in the Fe-FeS system under moderate pressure: Tool box to model small planetary cores. *American Mineralogist*, 103, 1770–1779.
- Mori, Y., Ozawa, H., Hirose, K., Simmyo, R., Tateno, S., Morard, G., and Ohishi, Y. (2017) Melting experiments on Fe-Fe₃S system to 254 GPa. *Earth and Planetary Science Letters*, 464, 135–141.
- Murthy, V.R., and Hall, H.T. (1970) The chemical composition of the Earth's core: Possibility of sulphur in the core. *Physics of the Earth and Planetary Interiors*, 2, 276–282.
- Nishida, K., Ohtani, E., Urakawa, S., Suzuki, A., Sakamaki, T., Terasaki, H., and Katayama, Y. (2011) Density measurement of liquid FeS at high pressures using synchrotron X-ray absorption. *American Mineralogist*, 96, 864–868.
- Norman, N. (1957) The Fourier transform method for normalizing intensities. *Acta Crystallographica*, 10, 370–373.
- Péters, M.J., Le Maistre, S., Yseboodt, M., Marty, J.C., Rivoldini, A., Van Hoolst, T., and Dehant, V. (2020) LaRa after RISE: Expected improvement in the Mars rotation and interior models. *Planetary and Space Science*, 180, 104745.
- Petříček, V., Dušek, M., and Palatinus, L. (2014) Crystallographic computing system JANA2006: General features. *Zeitschrift für Kristallographie—Crystalline Materials*, 229, 345–352.
- Seto, Y., Nishio-Hamane, D., Nagai, T., and Sata, N. (2010) Development of a software suite on X-ray diffraction experiments. *The Review of High Pressure Science and Technology*, 20, 269–276.
- Stewart, A.J., Schmidt, M.W., van Westrenen, W., and Liebske, C. (2007) Mars: A new core-crystallization regime. *Science*, 316, 1323–1325.
- Sun, D.Y., Asta, M., and Hoyt, J.J. (2004) Crystal-melt interfacial free energies and mobilities in fcc and bcc Fe. *Physical Review B*, 69, 174103.
- Tateno, S., Komabayashi, T., Hirose, K., Hirao, N., and Ohishi, Y. (2019) Static compression of B2 KCl to 230 GPa and its PVT equation of state. *American Mineralogist*, 104, 718–723.
- Terasaki, H., Rivoldini, A., Shimoyama, Y., Nishida, K., Urakawa, S., Maki, M., Kurokawa, F., Takubo, Y., Shibasaki, Y., Sakamaki, T., and others (2019) Pressure and composition effects on sound velocity and density of core-forming liquids: Implication to core compositions of terrestrial planets. *Journal of Geophysical Research: Planets*, 124, 2272–2293.
- Thompson, S., Komabayashi, T., Breton, H., Suehiro, S., Glazyrin, K., Pakhomova, A., and Ohishi, Y. (2020) Compression experiments to 126 GPa and 2500 K and thermal equation of state of Fe₃S: Implications for sulphur in the Earth's core. *Earth and Planetary Science Letters*, 534, 116080.
- Tsujino, N., Nishihara, Y., Nakajima, Y., Takahashi, E., Funakoshi, K.I., and Higo, Y. (2013) Equation of state of γ -Fe: Reference density for planetary cores. *Earth and Planetary Science Letters*, 375, 244–253.
- Yoder, C.F., Konopliv, A.S., Yuan, D.N., Standish, E.M., and Folkner, W.M. (2003) Fluid core size of Mars from detection of the solar tide. *Science*, 300, 299–303.

MANUSCRIPT RECEIVED DECEMBER 9, 2020

MANUSCRIPT ACCEPTED AUGUST 4, 2021

MANUSCRIPT HANDLED BY RYOSUKE SINMYO

Endnote:

¹Deposit item AM-22-77924, Online Materials. Deposit items are free to all readers and found on the MSA website, via the specific issue's Table of Contents (go to http://www.minsocam.org/MSA/AmMin/TOC/2022/Jul2022_data/Jul2022_data.html). The CIF has been peer reviewed by our Technical Editors.